WILEY

RESEARCH ARTICLE

Diurnal cycle RANS simulations applied to wind resource assessment

Jordi Barcons ⓘ | Matias Avila ⓘ | Arnau Folch ⓘ

Barcelona Supercomputing Center (BSC), Barcelona, Spain

Correspondence
Jordi Barcons, Barcelona Supercomputing Center (BSC), Nexus II Building, Jordi Girona, 29, 08034 Barcelona, Spain.
Email: jordi.barcons@bsc.es

Abstract

Microscale computational fluid dynamics (CFD) models can be used for wind resource assessment on complex terrains. These models generally assume neutral atmospheric stratification, an assumption that can lead to inaccurate modeling results and to large uncertainties at certain sites. We propose a methodology for wind resource evaluation based on unsteady Reynolds averaged Navier-Stokes (URANS) simulations of diurnal cycles including the effect of thermal stratification. Time-dependent boundary conditions are generated by a 1D precursor to drive 3D diurnal cycle simulations for a given geostrophic wind direction sector. Time instants of the cycle representative of four thermal stability regimes are sampled within diurnal cycle simulations and combined with masts time series to obtain the wind power density (WPD). The methodology has been validated on a complex site instrumented with seven met masts. The WPD spatial distribution is in good agreement with observations with the mean absolute error improving 17.1% with respect to the neutral stratification assumption.

KEYWORDS

diurnal cycle, thermal effects, thermal stability, wind resource assessment, wind power density

1 | INTRODUCTION

Microscale atmospheric models are widely used in wind energy for wind resource assessment (WRA) and wind turbine siting (eg, Ayotte[1]). In the case of onshore sites, simple linear models like WAsP[2] or MS-Micro[3] are still in use by the industry. Such models are based on simplified equations of motion, where the advection and turbulent terms are linearized. However, linear models are not able to correctly solve flow separation and recirculation effects often occurring in complex terrain.[4] This motivates the use of more complex engineering computational fluid dynamics (CFD), typically built on the Reynolds averaged Navier-Stokes (RANS) equations. Several RANS turbulence models (eg, $k - l$, $k - \epsilon$, $k - \omega$, etc) have been adapted to simulate atmospheric boundary layer (ABL) flows under neutral stratification (eg, Avila et al[5]), although neutral atmospheric conditions are rarely observed in the real world.[1,6] Over land, the ABL undergoes strong diurnal variations in response to surface forcings, eg, frictional drag, terrain orography, and solar heating. The cycle of insolation is intrinsically dynamic and entails large variations in quantities relevant to WRA like wind speed and direction or turbulence. In order to account for these thermal effects, microscale RANS models need to be coupled with the energy conservation equation. Examples of thermally coupled RANS models can be found in Pieterse et al[7] and Koblitz et al.[8] Both studies simulated thermal stratification effects on the flow field and compared reasonably well with observations. In particular, Koblitz et al[8] implemented the thermal model of Sogachev et al[9] in the CFD solver EllipSys3D. Sogachev's model has the advantage that it does not introduce additional coefficients, being suitable for any set of k-ϵ model coefficients.

Two main approaches exist in the literature to prescribe time-dependent boundary conditions for thermally stratified RANS models in ABL simulations. The first option consists of coupling dynamically with a mesoscale model. For example, Castro et al[10] and Rodrigues et al[11] coupled the microscale models WINDIE and VENTOS with the WRF mesoscale model. Such dynamical downscaling strategies were able to simulate real

atmospheric conditions and provided improvements in the wind speed predictions with respect to the mesoscale model results. However, given its higher computational cost, dynamical downscaling methodologies are still unpractical for WRA. The second option consists on prescribing inflow profiles already stratified. For example, Pieterse et al[7] prescribed steady inflow profiles, and Koblitz et al[8] used a 1D precursor to provide time-dependent boundary conditions to EllipSys3D. Here, we adopt this second approach because of its general applicability and simplicity.

During WRA studies, RANS simulations for discretized inflow wind direction sectors are used to expand scattered mast observations of wind distributions over the entire region of interest (RoI). To this end, model wind speedups and rota tions using a reference mast are frequency weighed to transport mast annually averaged observations to any point of the domain. This paper proposes a methodology for WRA based on diurnal cycle (DC) RANS simulations that introduce thermal stability as an additional parameter in the process. Section 2 presents the Alya-CFDWind microscale wind model, in which the thermal model of Sogachev et al[9] has been implemented to simulate a thermally stratified ABL. Section 3 describes the methodology to run 3D DC simulations in complex terrains. Section 4 outlines our WRA methodology, including the DC discretization using ABL stability classes, and applies the results obtained in section 3 to estimate the wind power density (WPD). Results using the classical neutral stratification assumption and the proposed DC methodology are compared with observations from met masts. Finally, section 5 presents the conclusions and discusses on future improvements of our methodology.

2 | ALYA-CFDWIND THERMAL MODEL

2.1 | Governing equations

Alya-CFDWind[5,12] is a CFD code for the ABL implemented in Alya, a High Performance Computing multiphysics parallel solver based on the finite element method.[13,14] In order to consider atmospheric stability and Coriolis forces, we have implemented the thermal model of Sogachev et al.[9] The resulting Alya-CFDWind model equations are the incompressible unsteady Reynolds averaged Navier-Stokes (URANS) Equations 1 to 2, together with a k-ϵ turbulence model (3) to (4) and the energy conservation Equation 5. The model uses the Boussinesq approximation for thermal coupling in the momentum equation. Sogachev's model uses a maximum mixing length limitation model initially proposed by Apsley and Castro.[15] The resulting system of equations yields:

$$\nabla \cdot \mathbf{u} = 0, \tag{1}$$

$$\frac{\partial \mathbf{u}}{\partial t} + \mathbf{u} \cdot \nabla \mathbf{u} - \nabla \cdot \left(\nu_t \nabla^s \mathbf{u} \right) = -\boldsymbol{\nabla} p - f_c \mathbf{e_z} \times \mathbf{u} - \mathbf{g} \frac{\theta}{\theta_0}, \tag{2}$$

$$\frac{\partial k}{\partial t} + \mathbf{u} \cdot \nabla k - \nabla \cdot \left(\frac{\nu_t}{\sigma_k} \cdot \nabla k \right) = P_k - \epsilon + G_k, \tag{3}$$

$$\frac{\partial \epsilon}{\partial t} + \mathbf{u} \cdot \nabla \epsilon - \nabla \cdot \left(\frac{\nu_t}{\sigma_\epsilon} \cdot \nabla \epsilon \right) = \frac{\epsilon}{k} \left[\left(C_1 + (C_2 - C_1) \frac{l_m}{l_{max}} \right) P_k - C_2 \epsilon + C_3 G_k \right], \tag{4}$$

$$\frac{\partial \theta}{\partial t} + \mathbf{u} \cdot \nabla \theta - \nabla \cdot \left(\frac{\nu_t}{\sigma_\theta} \cdot \nabla \theta \right) = 0, \tag{5}$$

where the unknowns are the wind velocity $\mathbf{u}$, the pressure p, the turbulent kinetic energy k, the dissipation rate ϵ, and the potential temperature θ fields. The turbulent viscosity is given by $\nu_t = C_\mu k^2/\epsilon$, ∇^s is the symmetric gradient operator, and $f_c \mathbf{e_z} \times \mathbf{u}$ is the Coriolis force term, being $f_c = 2\Omega \sin \lambda$ the Coriolis parameters (with the Earth's rotation rate Ω and the latitude λ) and e_z a unit vector pointing to the vertical direction. The mixing length l_m and the maximum mixing length l_{max} are computed as

$$l_m = C_\mu^{3/4} \frac{k^{3/2}}{\epsilon}, \tag{6}$$

$$l_{max} = \beta \frac{\int_0^\infty z \sqrt{k} dz}{\int_0^\infty \sqrt{k} dz}, \tag{7}$$

where β is a coefficient chosen such in a neutrally stratified atmosphere $l_{max} = l_0$. Here, l_0 is the Blackadar length

$$l_0 = 0.0027 \frac{|\mathbf{u_g}|}{f_c},$$

where u_g is the geostrophic wind velocity. Sogachev et al[9] found that the empirical value of $\beta = 0.075$ in expression 7 agrees reasonably well ($l_{max} \approx l_0$). The turbulent kinetic energy production rates by mechanical shear (P_k) and buoyant forces (G_k) are, respectively,

$$P_k = 2\nu_t \overset{s}{\nabla}\mathbf{u} : \overset{s}{\nabla}\mathbf{u}, \tag{8}$$

$$G_k = -\alpha |\mathbf{g}| \frac{\nu_t}{\sigma_\theta} \frac{\partial \theta}{\partial z}, \tag{9}$$

where α is the thermal expansion coefficient ($\alpha = 1/\theta_0$ for ideal gases, being $\theta_0 = 298.0$ K the reference potential temperature), and σ_θ is the turbulent Prandtl number. Table 1 lists the model coefficients (from Panofsky and Dutton[16]) including the expression for C_3 depending on the stability-related function α_G[9] that, at the same time, depends on the local flux Richardson number $Ri = -G_k/P_k$ as

$$\alpha_G = \begin{cases} (1 - l_m/l_{max}) & \text{for } Ri > 0 \quad \text{(Stable)} \\ 1 - (1 + (C_2 - 1)/(C_2 - C_1)) l_m/l_{max} & \text{for } Ri < 0 \quad \text{(Unstable)}. \end{cases} \tag{10}$$

TABLE 1 Alya-CFDWind thermal model constants[16]

κ	C_μ	C_1	C_2	C_3		σ_k	σ_ϵ	σ_θ
0.41	0.033	1.176	1.92	$1 + (C_1 - C_2)\alpha_G$		1.0	1.238	0.9

2.2 | Boundary conditions

The Alya-CFDWind model Equations 1 to 5 must be supplied with initial and boundary conditions. The boundaries of the computational domain are classified into bottom, top, lateral inflow, and lateral outflow.

- **On the bottom boundary**, wall law functions are imposed to verify the Monin-Obukhov similarity theory[17] for momentum, energy, and turbulence equations. The imposed shear stress τ_{wall} and boundary heat flux q_w are related to the wind velocity and potential temperature at a distance δ_w from the ground (wall distance), as follows:

$$\boldsymbol{\tau_w} = -u_{*v}u_{*k}\frac{\mathbf{u}(\delta_w)}{|\mathbf{u}(\delta_w)|}, \tag{11}$$

$$\theta(\delta_w) - \theta_{wall} = \frac{\sigma_t\theta_*}{\kappa}\left[\ln\left(1 + \frac{\delta_w}{z_0}\right) - \Psi_h\left(\frac{\delta_w}{L}\right)\right], \tag{12}$$

where z_0 is the terrain roughness length, θ_{wall} is the potential temperature at the wall, and κ is the Von Karman constant ($\kappa = 0.41$). The two scale friction velocities u_{*v} and u_{*k} are based on the velocity modulus and turbulent kinetic energy, respectively, being defined as follows:

$$|\mathbf{u}(\delta_w)| = \frac{u_{*v}}{\kappa}\left[\ln\left(1 + \frac{\delta_w}{z_0}\right) - \Psi_m\left(\frac{\delta_w}{L}\right)\right]$$

$$u_{*k} = C_\mu^{1/4}k(\delta_w)^{1/2}$$

The friction potential temperature is $\theta_* = q_{wall}/\rho c_p u_{*k}$, where q_{wall} is the downwards surface heat flux, c_p is the heat capacity, and ρ is the air density. The correction terms $\Psi_m(\delta_w/L)$ and $\Psi_h(\delta_w/L)$ account for thermal stability and are functions of the ratio δ_w/L, where L is the Obukhov length ($L = u_{*v}^2/\kappa\alpha|\mathbf{g}|\theta_*$). For the turbulent kinetic energy, a zero diffusion through the wall is imposed (ie, $\nabla k \cdot \mathbf{n} = 0$, where $\mathbf{n}$ is the wall outwards normal vector). The dissipation rate at δ_w is imposed to verify equilibrium as

$$\epsilon(\delta_w) = \frac{u_{*k}^3}{\kappa(\delta_w + z_0)}. \tag{13}$$

- **On the top boundary**, symmetry boundary conditions (zero normal gradient) are imposed for the tangential velocity component, θ, k, and ϵ. The normal velocity component is prescribed to zero (ie, $\mathbf{u} \cdot \mathbf{n} = 0$).
- **On the inflow boundary**, vertical profiles for $\mathbf{u}$, θ, k, and ϵ are imposed from a precursor simulation (see section 3.1) assuming uniform roughness and flat terrain.
- **On the outflow boundary**, symmetry boundary conditions are imposed for θ, k, and ϵ. For the momentum equation, two options exist, to impose the geostrophic pressure and no shear stress or to prescribe the velocity vertical profiles (ie, to impose Dirichlet conditions at the outflow). The advantages/drawbacks of each option are discussed in section 3.

3 | DC SIMULATION

The simulation of a DC on complex terrain implies the preprocess, the AlyaCFD-Wind simulation and the postprocess. A set of preprocessing software tools assimilate terrain information, generate a structured mesh (see Gargallo-Peiró et al[18,19] for details) and impose initial and time-dependent boundary conditions (IC and Boundary Conditions (BC)). The present work assumes that the computational meshes are composed by hexahedral elements and have three differentiated regions: an external flat buffer (used to accommodate the inflow BCs and to avoid recirculation at the outflow boundary), an adjacent transition zone, and an inner higher-resolution zone, henceforth called RoI. The IC and BCs are generated by means of a 1D precursor model that assumes uniform roughness and flat terrain.[5]

3.1 | The 1D precursor model

The Alya-CFDWind 1D precursor model is a single-column model that assumes flat terrain and horizontally homogeneous flows. This precursor model is used to obtain vertical profiles of the unknowns, which are later imposed as IC and BCs to Alya-CFDWind. To simulate a DC, the precursor model needs as BCs a time-varying wall temperature (or surface heat flux) and a geostrophic wind at top.

The precursor model was validated against the GABLS2 benchmark,[20] a challenging case of strong DC over dry land. To facilitate the model intercomparison in Svensson et al,[20] the forcing conditions (driving the DC) were simplified giving rise to an "idealized" case that considered a constant geostrophic wind velocity of $|\mathbf{u}_g| = 9.5$ ms^{-1}. In addition to GABLS2, we also introduced a modified version of the benchmark, henceforth called CYCLE. This consists of a periodic repetition of the boundary conditions of the first day in GABLS2. The CYCLE is meant to guarantee that, after enough simulation time, the results of the 1D precursor model are cyclic and independent of the initial condition (IC). Figure 1 shows time-varying surface temperatures of both DCs (GABLS2 and CYCLE), used as the bottom condition for the 1D Alya-CFDWind precursor model.

Figure 2 shows 1D precursor model vertical profiles at noon (thermally unstable) and midnight (thermally stable). Note that the CYCLE periodic run needed five cycles to achieve periodicity. As expected, the unstable and stable regimes show large differences. For example, the nocturnal boundary layer (NBL) height is slightly above 100 m, contrasting with the 1-km ABL height at noon. Furthermore, there is a relatively high and well-defined nocturnal low-level jet of about $\mathbf{u} = 12$ ms^{-1} at the top of the NBL. This contrasts with the $\mathbf{u} = 6.5$ ms^{-1} at the same height during the unstable regime (as seen in Sanz-Rodrigo et al[21]). Turbulent kinetic energy also shows large differences, specially until a height of 100 m.

Figure 3 compares precursor near-surface results (GABLS2 and CYCLE) with those from the large eddy simulation (LES) in Kumar et al[22] and the RANS single-column models (SCMs) spread from Svensson et al.[20] It is observed that GABLS and CYCLE runs obtain very similar results
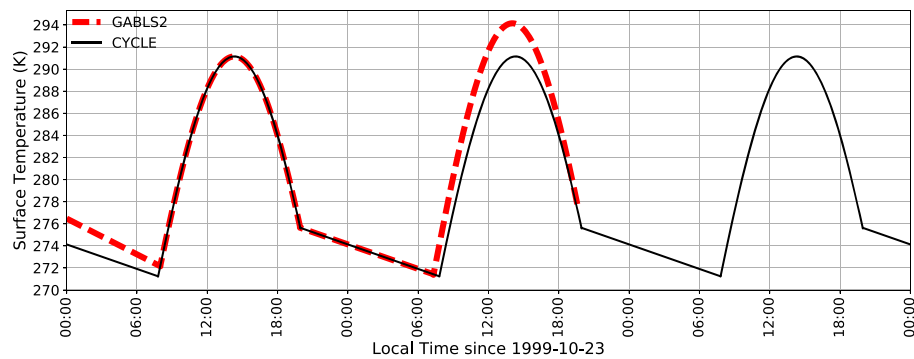

FIGURE 1 Time series of surface temperature for GABLS2 and CYCLE 1D diurnal cycles. The GABLES2 benchmark actually starts on 22 October 1999 at 16 hours local time (LT) allowing 8 hours of spin-up. The 23 October 1999 is selected as the evaluation period and is the segment that is repeated in the periodic CYCLE [Colour figure can be viewed at wileyonlinelibrary.com]
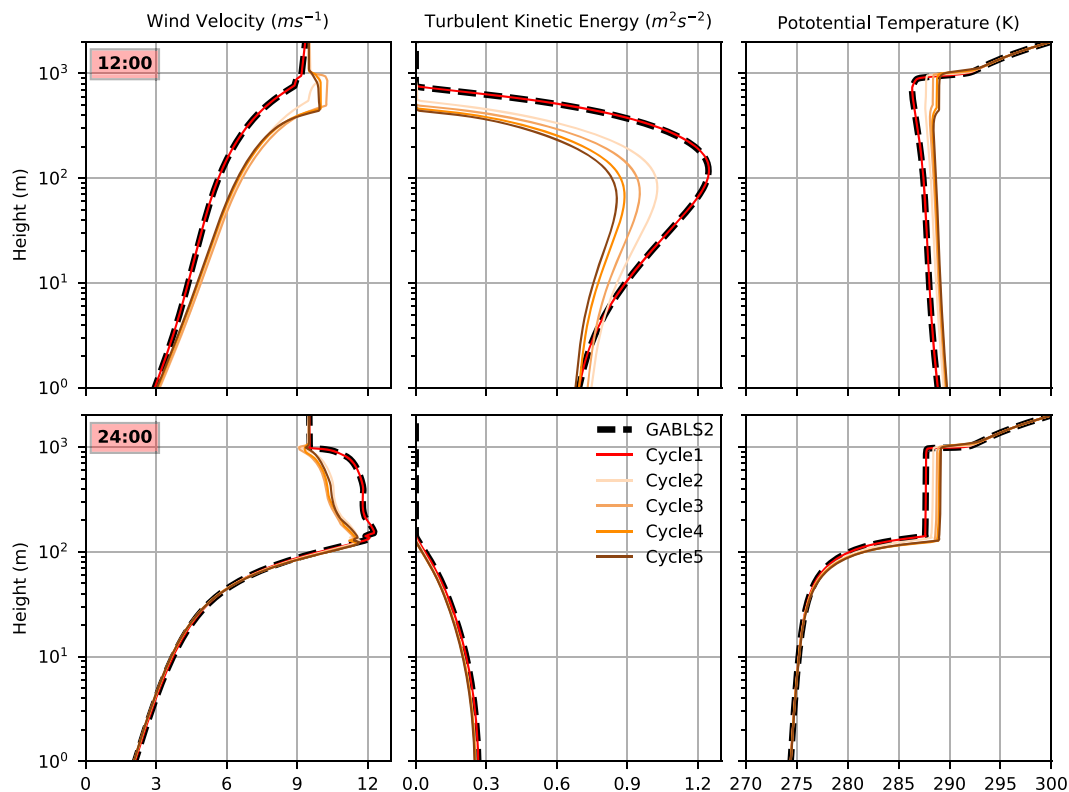

FIGURE 2 Vertical profiles of wind velocity, turbulent kinetic energy, and potential temperature at 12:00 (top) and at 24:00 local time (LT) (bottom) for GABLS2 and CYCLE (five consecutive periodic cycles Cycle 1 to Cycle 5 are shown) [Colour figure can be viewed at wileyonlinelibrary.com]
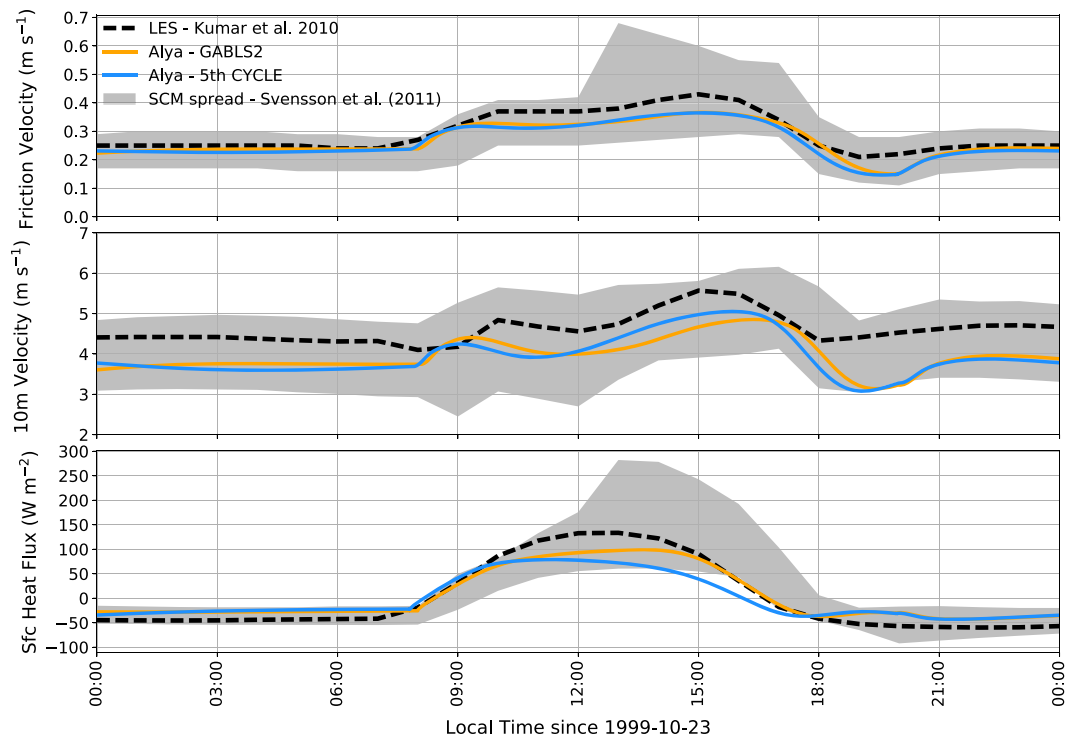
FIGURE 3 GABLS2 23 October 1999 time series of friction velocity (top), 10-m wind velocity (middle), and surface heat flux (bottom). Comparison between large eddy simulation (LES) simulation from Kumar et al,[22] our precursor model (GABLS2 and Cycle5 results), and the single-column model (SCM) spread reported in Svensson et al[20] [Colour figure can be viewed at wileyonlinelibrary.com]

during night time and slightly differ during day time. These differences between the precursor and the LES model appear in the 10-m wind velocity and surface heat flux (Figure 3). Despite this, the precursor results lay within the spread of the SCMs.

3.2 | Alya-CFDWind simulations

We consider a very complex terrain site located in the Mexican state of Puebla. This site was intensively monitored during a wind resource assessment campaign by a private company that gave us access to a part of the long-period dataset acquired. This dataset consisted on 80 m height wind measurements from seven met masts instrumented with sonic anemometers for a total period of acquisition of 3 years.

3.2.1 | Mesh setup

For the Puebla case, we defined a domain with an inner RoI of $6.4 \times 13 \text{ km}^2$ as shown Figure 4. In this inner part, the horizontal grid resolution was set to $\delta x = \delta y = 100$ m. Around it, we used a gradually increasing element size (transition zone) until the buffer zone. The transition and buffer regions (Figure 4) are 1 and 50 km long, respectively. The buffer needs to be long to impose the outflow boundary conditions far enough of the RoI. In the vertical direction, the grid has 60 vertical layers growing geometrically in size inside the ABL (up to ~ 1000 m height) from 1 to 170 m. The top of the mesh was placed at 2.4 km above the highest terrain elevation.

3.2.2 | Precursor simulation

We ran the 1D precursor simulation with the CYCLE time-varying surface temperature (as in section 3.1), with a geostrophic wind velocity of $|\mathbf{u}_g| = 17.5 \text{ ms}^{-1}$ and the Coriolis factor $f_c = 4.5 \times 10^{-5} \text{ s}^{-1}$, corresponding to a latitude 18°. The increment of $|\mathbf{u}_g|$ with respect to the GABLS2 benchmark ($|\mathbf{u}_g| = 9.5 \text{ ms}^{-1}$) was introduced to reduce the Coriolis and the thermal coupling effects, reducing the numerical complexity of the Alya-CFDWind simulation. From dimensionless analysis, the influence on the flow of the Coriolis and thermal terms depend, respectively, on f_c/u_g and $1/L$. Therefore, these effects decrease when the characteristic velocity $\mathbf{u}_g$ is increased.

3.2.3 | Boundary conditions

In the case of steady-state neutral simulations, Alya-CFDWind BCs consist on prescribed inflow vertical profiles, outflow symmetric BCs for k and ϵ, and geostrophic pressure and no shear stress for the momentum equation at the outflow boundary (section 2.2). In contrast, during DC thermal simulations, inflow and outflow BCs change over time. Inflow BCs consist of vertical profiles coming from the 1D precursor model. Outflow
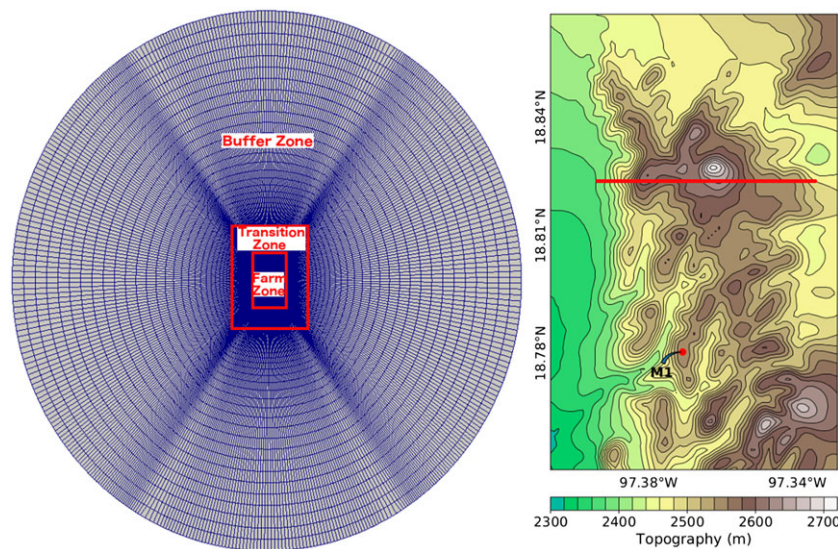
FIGURE 4 Puebla test case. Horizontal mesh representation with the inner part colored (left) and a zoom of the inner region of interest (Farm Zone) at 100-m resolution (right) showing contours of topography. The computational mesh has 1.6 million nodes. The horizontal red line marks the longitudinal cut used in further plots, and M1 is the reference mast used for wind resource assessment (WRA) [Colour figure can be viewed at wileyonlinelibrary.com]

BCs are still symmetric for θ, k, and ϵ. However, when the geostrophic pressure is imposed on the outflow boundary as in the neutral case, the differences between the pressure of the flow reaching the outflow and the prescribed pressure generate significant recirculations that can destabilize the simulation. As the temperature profile at the outflow boundary is not known a priori, it is not possible to prescribe an appropriate outflow pressure. An alternative to avoid imposing the pressure at the outflow, is to prescribe vertical profiles for **u** (Dirichlet outflow condition). This type of outflow condition is not frequently used in complex terrain simulations because it produces numerical oscillations near the outflow wall. We circumvented this issue by placing the outflow boundary more than 50 km downwind from the RoI. This strategy guarantees that the flow field has almost recovered the flat terrain shape structure when reaching the outflow, so that the oscillations generated are spurious and localized in the buffer region.

3.2.4 | Time integration step

The 1D precursor profiles are imposed over the whole domain as ICs. In order to accommodate these ICs, we used a small integration time step of $\delta t = 0.15$ s (which led to a Courant number $C \approx 1$) during the first 200 time integration steps. Then, we increased δt progressively up to a value of $\delta t = 6$ s, which remained constant until the end of the simulation. The obtained Courant number (C) varied between $C = 40$ and $C = 90$ when using $\delta t = 6$ s. These values justifies the implicit discretization of the equations. Each DC for the Puebla case needed approximately 24 times the number of CPU hours needed for the neutral simulation.

3.2.5 | Results

Figure 5 shows Puebla contour plots across a longitudinal vertical cut plane (red line in the right plot of Figure 4) for u_x, k, and θ considering a geostrophic wind direction of 270° and for two time instants, at 2 (thermally stable) and at 14 hours (thermally unstable) local time (LT). The figure shows also vertical profiles at four different locations (white lines in the vertical cuts) to highlight differences between both time instants.

Large u_x vertical gradients are observed in the 2 hours LT plots, favored by the strong stable thermal stratification. In this situation, the large θ vertical gradients inhibit the vertical mixing and the resulting homogenization of the NBL. The top of the NBL is slightly above 2.8 km asl (around 400 m above the lowest terrain height in the figure). At this height, large values of u_x denote a low-level jet of around $u_x \approx 20$ ms^{-1}. The blocking effect of the hills, which enhance the production of k in the jet with a peak up to $k \approx 4$ m^{2}s^{-2}, are also visible. Note that, just above the NBL, k drops and almost vanishes. Note also that the flow is not allowed to go uphill and recirculates on the left part of the u_x plot (u_x shows negative values near the surface). These stable stratified plots contrast significantly with the plots at 14 hours LT. At this time, the θ plots show an ABL thermally unstable that enhances vertical mixing and favors a well-mixed ABL. The θ and k vertical profiles indicate that the top of the ABL is at around 3.4 km asl (around 1000 m above the lowest terrain height in the figure). The vertical profiles of u_x are smooth and gradually grow with height near the top of the hills. The turbulent kinetic energy k has its maximum near the surface and decreases gently with height.
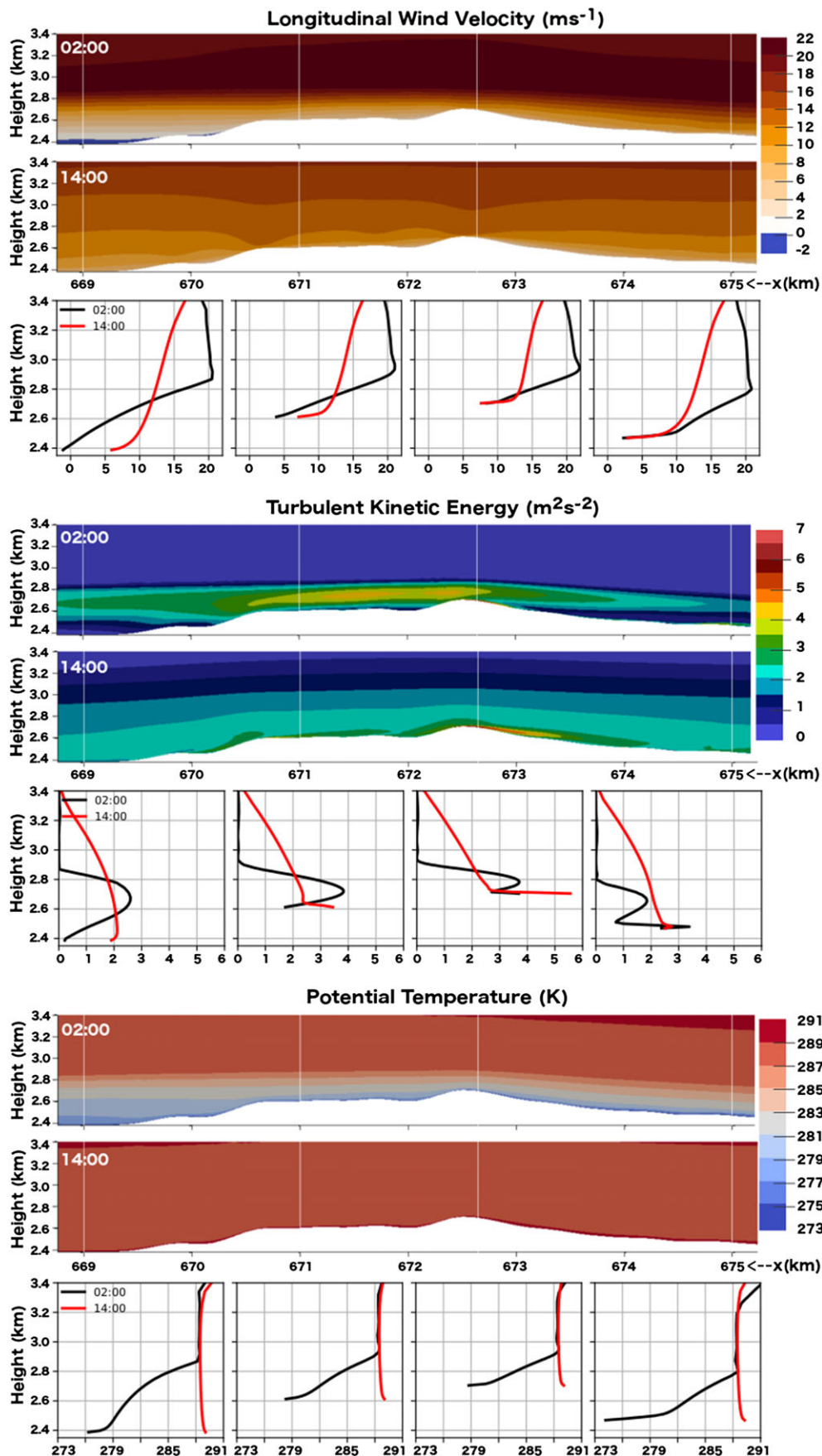
FIGURE 5   Contour plots and vertical profiles at four sites (marked with thin vertical white lines) at 2 hours (thermally stable) and 14 hours (thermally unstable) local time (LT) for longitudinal velocity u_x (top), turbulent kinetic energy k (middle), and potential temperature θ (bottom) along the 6 km length cross section shown in Figure 4. Results for the diurnal cycle simulation with a geostrophic wind direction of 270°, ie, aligned with the x axis [Colour figure can be viewed at wileyonlinelibrary.com]

4 | WIND RESOURCE ASSESSMENT

The classical neutral-based WRA methodology classifies near-surface wind time series from met masts into wind direction sectors and velocity bins. Microscale simulations accounting for terrain effects are then used to extrapolate measurements over the RoI and to obtain yearly averaged quantities of interest like mean wind speed or WPD. In this classical approach, the number of simulations can vary depending on the number of wind direction sectors used.

4.1 | Methodology to include thermal stability

DC simulations introduce a third component in addition to wind direction and velocity, the thermal stability class. This requires a classification of the observed wind time series into thermal stability classes to generate three-dimensional wind roses.

4.1.1 | Classification of wind time series into thermal stability classes

Ideally, a WRA measuring campaign should have heat flux and temperature sensors at different heights to construct a long-period (yearly) wind rose for each thermal stability class. Unfortunately, the Puebla dataset does not contain either heat fluxes nor temperature measurements. This limitation forced us to define a methodology to extract thermal stability classes using mesoscale simulations for the evaluation period. We used the mesoscale Weather Research and Forecasting model[23] (WRF; see Table 2 for model setup) outputs as a virtual mast for the RoI. The WRF model provided ground heat fluxes (H_G) and surface heat fluxes (H_S), and we also diagnosed the static thermal stability ($\Delta\theta/\Delta z$) using 5 and 100 m height potential temperatures (θ). Ground heat fluxes H_G were used because they showed a good agreement with day-night alternation ($H_G < 0$ W·m^{-2} and $H_G > 0$ W·m^{-2}, respectively). All quantities were space averaged over the WRF points inside RoI at the same level (the RoI contains 3×5 WRF grid points in each horizontal plane). The Obukhov length from WRF was not used because the obtained values were very heterogeneous inside the RoI. Four different stability classes (stable, stable-to-unstable transition, unstable, and unstable-to-stable transition) were delimited as defined in the following scheme:

$$H_G \begin{cases} < 0.0\text{W} \cdot \text{m}^{-2} \text{ and } \Delta\theta/\Delta z \begin{cases} > 1.0\text{K} \cdot \text{km}^{-1} \text{ and } H_S \begin{cases} < 0.0\text{W} \cdot \text{m}^{-2} \to \textbf{Stable} \\ > 0.0\text{W} \cdot \text{m}^{-2} \to \textbf{Unstable to Stable} \end{cases} \\ < -1.0\text{K} \cdot \text{km}^{-1} \text{ and } H_S \begin{cases} > 0.0\text{W} \cdot \text{m}^{-2} \to \textbf{Unstable} \\ < 0.0\text{W} \cdot \text{m}^{-2} \to \textbf{Unstable to Stable} \end{cases} \\ 1.0\text{K} \cdot \text{km}^{-1} > \Delta\theta/\Delta z > -1.0\text{K} \cdot \text{km}^{-1} \to \textbf{Unstable to Stable} \end{cases} \\ > 0.0\text{W} \cdot \text{m}^{-2} \text{ and } \Delta\theta/\Delta z \begin{cases} < -1.0\text{K} \cdot \text{km}^{-1} \text{ and } H_S > 0.0\text{W} \cdot \text{m}^{-2} \to \textbf{Unstable} \\ > -1.0\text{K} \cdot \text{km}^{-1} \to \textbf{Stable to Unstable} \end{cases} \end{cases}$$

4.1.2 | DC simulations and sampling of stability classes

For each DC simulation, our methodology selects one time instant as representative of each stability class. This criterion is simpler than a wind time-series classification because it builds on the idealized 1D precursor simulations that neglect atmospheric effects like humidity, latent heat, or

TABLE 2 Configuration and physical parameterizations of the WRF-ARW (version 3.4.1) model for the Puebla test case

| WRF-ARW configuration	
Model version	3.4.1
Initial and lateral BCs	Operational forecast deterministic ECMWF model at 0.125° resolution
Domains	1
Horizontal grid resolution	3 km
Horizontal grid size	86 × 86
Vertical levels	60 levels, with top at 50\,hPa
Simulation length	48 h (spin-up of 24 h)
Integration time step	20 s
WRF-ARW 3.4.1 physical schemes	
Microphysics	WRF single-moment 6-class (WSM6)[24]
Cumulus	Modified Kain-Fritsch[25]
Surface Layer	ETA Monin-Obukhov[26]
Land Surface	Unified Noah Land Surface Model (LSM)[27]
Planet Boundary Layer	Mellor Yamada Janjic (MYJ)[28]
Long-wave Radiation	Rapid Radiative Transfer Model (RRTM)[29]
Short-wave Radiation	Dudhia[30]
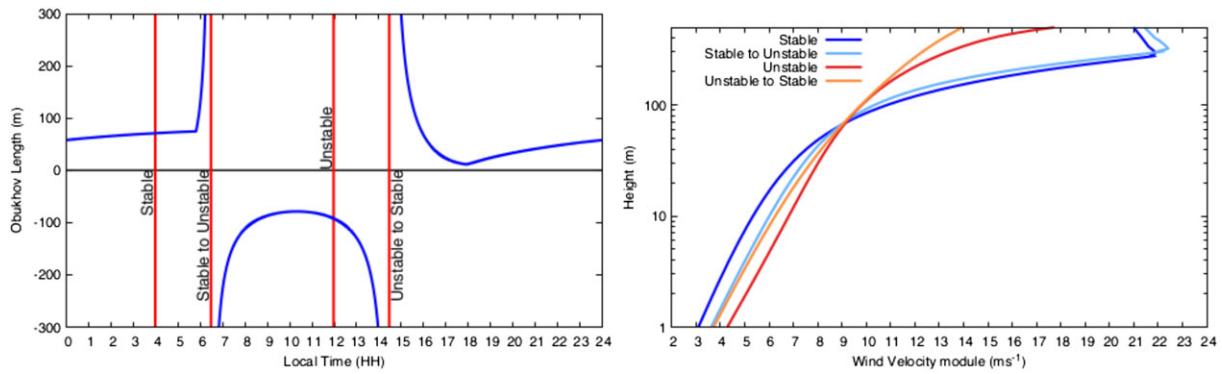
FIGURE 6 Left: Obukhov length time evolution of Cycle 5 diurnal cycle using Alya-CFDWind1D model. The red vertical lines indicate the time instants that are considered representative of each thermal stability class. Right: wind velocity vertical profiles for each stability class (logarithmic scale) [Colour figure can be viewed at wileyonlinelibrary.com]

mesoscale tendencies. In the 1D precursor runs, we consider the surface heat fluxes (H_S) and the Obukhov length (L) (at first 1D model element) to recognize and delimit stable and unstable regimes and their transitions considering

$$H_S \begin{cases} < 0\,W \cdot m^{-2} \text{ and } L < 200m & \rightarrow \textbf{Stable} \\ > 0\,W \cdot m^{-2} \text{ and } L > -200m & \rightarrow \textbf{Ustable} \\ = 0\,W \cdot m^{-2} \text{ and } L \rightarrow \pm\infty & \rightarrow \textbf{Transitions}. \end{cases} \tag{14}$$

Finally, we analyze the $|u|$ vertical profiles (first 100 m above terrain) to select the simulation time instant representative of stable and unstable regimes. The time instants selected are those representative of a period where the $|u|$ vertical profile remain constant for certain hours (2-3 hours). Left plot in Figure 6 shows the time evolution of L, with vertical lines denoting the time instants assumed representative of each thermal stability class. The right plot in Figure 6 shows the wind speed profiles up to 140 m during the selected time instants.

4.1.3 | Averaged wind speed-up and WPD

The final step of the WRA procedure consists of the calculation of the mean wind speed and the wind power fields for each thermal stability class. These results are later weighted according to the percentages of occurrence of each stability class to obtain the WPD and the annually averaged speed-ups. The WPD is defined as

$$WPD = \frac{1}{2}\rho \overline{|\mathbf{u}|^3}, \tag{15}$$

being ρ the air density, and $\overline{|\mathbf{u}|^3}$ the expected value for the cubic wind velocity.

4.2 | Results for the Puebla site

This section compares and validates WRA results at the Puebla site considering the classical neutral stratified (NS) methodology and the proposed DC methodology. We considered 16 evenly spaced sectors (one simulation every 22.5°) for each methodology to complete the WRA. The evaluation of both methodologies used approximately 1 year of wind measurements from seven masts (M1-M7) at 80 m height. M1 was selected as the reference mast to calculate relative quantities like the speed-up fields. Some of the obtained results are shown as normalized values because data are confidential and not publicly available. To this end, we normalized the WPD (WPD') field with respect to the mean WPD calculated by measurements at all masts:

$$WPD'(x, y) = \frac{WPD(x, y)}{\frac{1}{N} \sum_{n=1}^{N} WPD_n}, \tag{16}$$

where WPD_n is the WPD calculated using the wind velocity measurements in mast n, and N is the total number of masts. The normalized bias (NB; in %) of the simulated WPD ($WPD_{Simulated_n}$) at each mast (n) is defined as

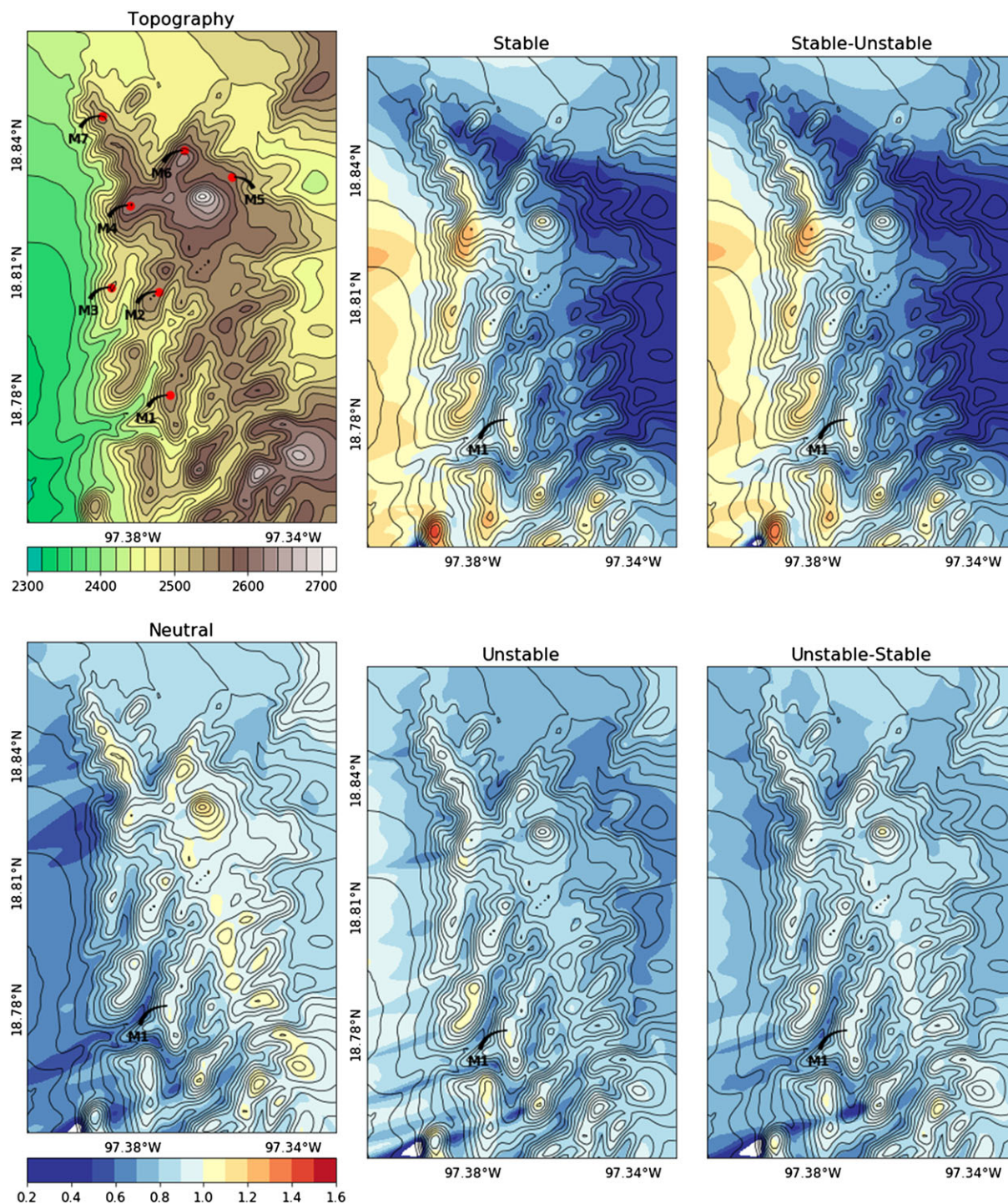$$NB_n = 100\% \left(\frac{WPD_{Simulated_n} - WPD_n}{WPD_n} \right). \tag{17}$$

FIGURE 7 Wind speed-up contour plots at 80 m above the terrain for the neutral case and the four stability classes. Simulations using a constant geostrophic wind direction of $\phi = 90°$ (ie, westward flow) and a geostrophic wind velocity of $|\mathbf{u}_g| = 17.5\,\text{ms}^{-1}$. The site has a preferential incoming wind direction of $\phi = 90° \pm 10°$ with around an 80 % of incidence per year. Speed-ups are relative to the reference mast M1. Contours of topography are shown for reference [Colour figure can be viewed at wileyonlinelibrary.com]

4.2.1 | Results for the 90° sector

The Puebla site has a preferential incoming wind direction of $\phi = 90° \pm 10°$ with around an 80% of occurrence. Figure 7 plots Alya-CFDWind results for the dominant 90° geostrophic wind direction, to compare the neutral model and the instants extracted from the DC, representative of each stability class. The plots in Figure 7 show the wind speed-ups relative to mast M1 at 80 m height. The neutral case shows that the wind speed increases with terrain elevation. However, this is not maintained in the stable and stable-to-unstable cases, which show a strong down-slope speed-up in the western part of the RoI favored by the strong nocturnal boundary layer stratification. Note that the stable and the stable-to-unstable plots present minor differences, suggesting that during stable stratification, the wind profiles remain quite unchanged regardless of the selected time instant. On the other hand, the wind speed-up fields in the unstable and the unstable-to-stable time instants are similar to the neutral case. The speed-up values are close to one on the RoI, and the down-slope effect is not observed.
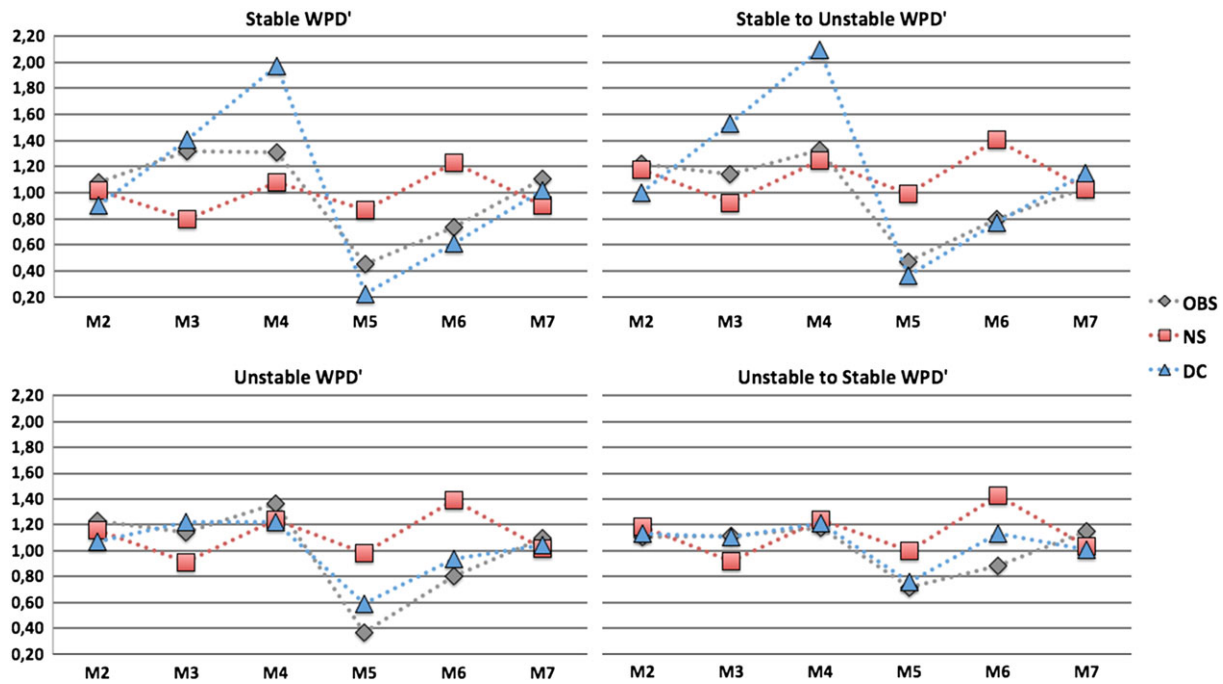
FIGURE 8 Validation at masts M2 to M7 using normalized WPD for each different thermal stability class. Observations in gray (OBS), results for the neutral case in red (NS), and results for the diurnal cycle strategy in blue (DC) [Colour figure can be viewed at wileyonlinelibrary.com]

4.2.2 | Wind power density obtained for each thermal stability class

Figure 8 shows the obtained WPD' (Equation 16) at the met masts for each stability class. This figure compares the predicted WPD' for NS and DC simulations against the WPD' calculated from wind measurements. It is seen that the DC WPD' predictions are in closer agreement with observations than the WPD' obtained using NS. This is true for all stability classes and over all masts with the only exception of M4 for stable cases. As it was observed in Figure 7, the unstable-to-stable DC class and the NS simulation predict a similar wind distribution.

4.2.3 | Wind power density results

Here, we compare the total WPD and mean speed-up obtained using DC and NS simulations. The DC methodology weighted each stability class using the percentages of occurrence obtained from WRF simulations: 37.0% stable, 8.5% stable-to-unstable transition, 28.0% unstable, and 26.5% unstable-to-stable transition. Figure 9 shows the ratios between the DC and the NS methodologies for the mean speed-up and the WPD at 80 m height. It is observed that the results present an east-west pattern, very similar to the stable case in Figure 7, because easterly winds are very prevalent (80% of direction frequency), and the stable stratification also dominates (37.0% of stability frequency).

Figure 10 presents the validation results of the DC and NS methodologies against WPD' values derived from observations. The left plot shows that the DC methodology highly improves the prediction of the WPD distribution at masts, showing an WPD' distribution much closer to observations. Note that M2 and M3 are installed in nearby hills (see right plot in Figure 9). There, NS simulations predict a higher WPD at M2 than at M3. However, measurements and the proposed thermal methodology show the opposite. On the right of Figure 10, the NB (Equation 17) of the DC and NS methodologies are shown with respect to the observations. The improvement of the DC methodology is evident observing this figure. In particular, a great improvement is observed at masts M3, M5, and M6, where the WPD NB is close to 50% for the neutral case and less than 22% for the DC. In addition, the mean absolute percentage error ($MAPE = \sum_n |NB_n|/N$) decreases from 30.1% to 13.0% respect to the classical neutral methodology.

4.2.4 | Sensitivity to the DC for the 90° sector

We studied the sensitivity of the obtained speed-ups to the DC considering three different cycles and the neutral case. Table 3 summarizes the four simulations considered. Cycle 1 is the DC described in section 3.2 (in the precursor simulation subsection) and used for all the previous results. Cycle 2 considers the same time-varying surface temperature as Cycle 1 and a lower geostrophic wind velocity $|\mathbf{u}_g| = 12\,ms^{-1}$. This reduction of geostrophic wind velocity increases the thermal coupling and Coriolis effects. Cycle 3 considers a reduced temperature amplitude ΔT_{wall} respect to Cycle 1 and the same geostrophic wind velocity $|\mathbf{u}_g| = 17.5\,ms^{-1}$. This ΔT_{wall} reduction reduces the thermal coupling effects. The most challenging case in terms of modeling was Cycle 2 due to the highest thermal coupling effects. Figure 11 shows the obtained speed-ups for each stability class at masts M2 to M7 for the dominant 90° sector. The most remarkable difference appears in the stable class, where Cycle 1 predicts a lower speed-up at M7 than the rest. It is also observed that Cycle 3 results are the most similar to neutral results due to the lower thermal coupling. In contrast, Cycle 2 speed-ups distribution in the unstable class differs most from the rest due to the higher thermal coupling effects. Despite these differences, the three cycles predict similar speed-up patterns.
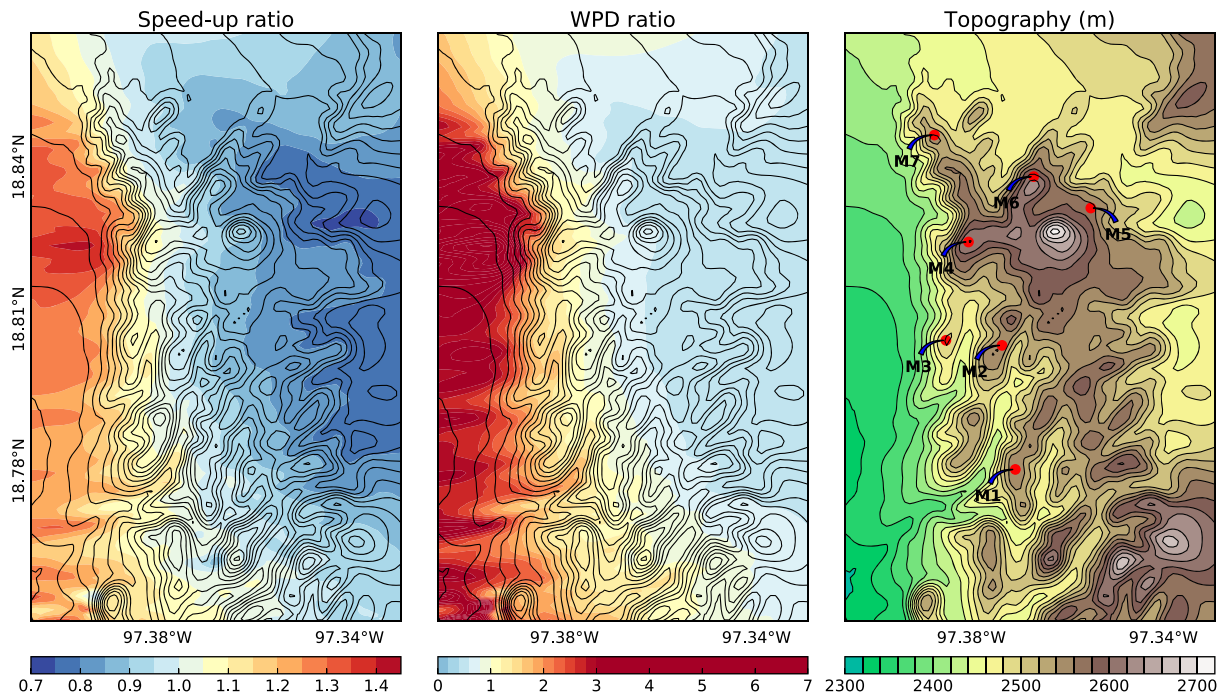
FIGURE 9   Left: the annual average speed-up ratio between the diurnal cycle and the neutral wind resource assessment (WRA) results at 80 m height. Middle: WPD ratio between the diurnal cycle and the neutral WRA results at 80 m height. Right: topography contours and locations of masts M1 to M7. Mast M1 is used as the reference for speed-up computation, and masts M2 to M7 are used for validation [Colour figure can be viewed at wileyonlinelibrary.com]
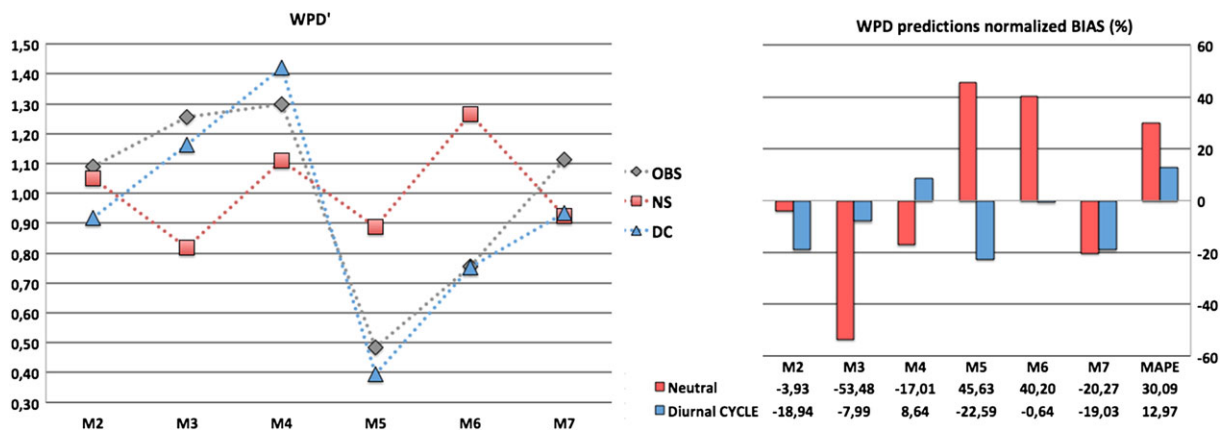

FIGURE 10   Left: validation at masts M2 to M7 using normalized wind power density (WPD) (Equation 16). Observations in gray (OBS), results for the neutral case in red (NS), and results for the diurnal cycle strategy in blue (DC). Right: normalized bias (Equation 17) at masts M2 to M7 for neutral (red) and diurnal cycle (blue) wind resource assessment (WRA) cases. The mean absolute percentage error (MAPE) for all masts are 30.09% and 12.97% for the neutral and diurnal cycle strategies, respectively [Colour figure can be viewed at wileyonlinelibrary.com]

TABLE 3   Summary of the diurnal cycles used in the sensitivity analysis[a]

Name	Daily ΔT_{wall} (K)	$|u_g|$ (ms^{-1})
Neutral	0.0	17.5
Cycle 1	19.8	17.5
Cycle 2	19.8	12.0
Cycle 3	13.5	17.5

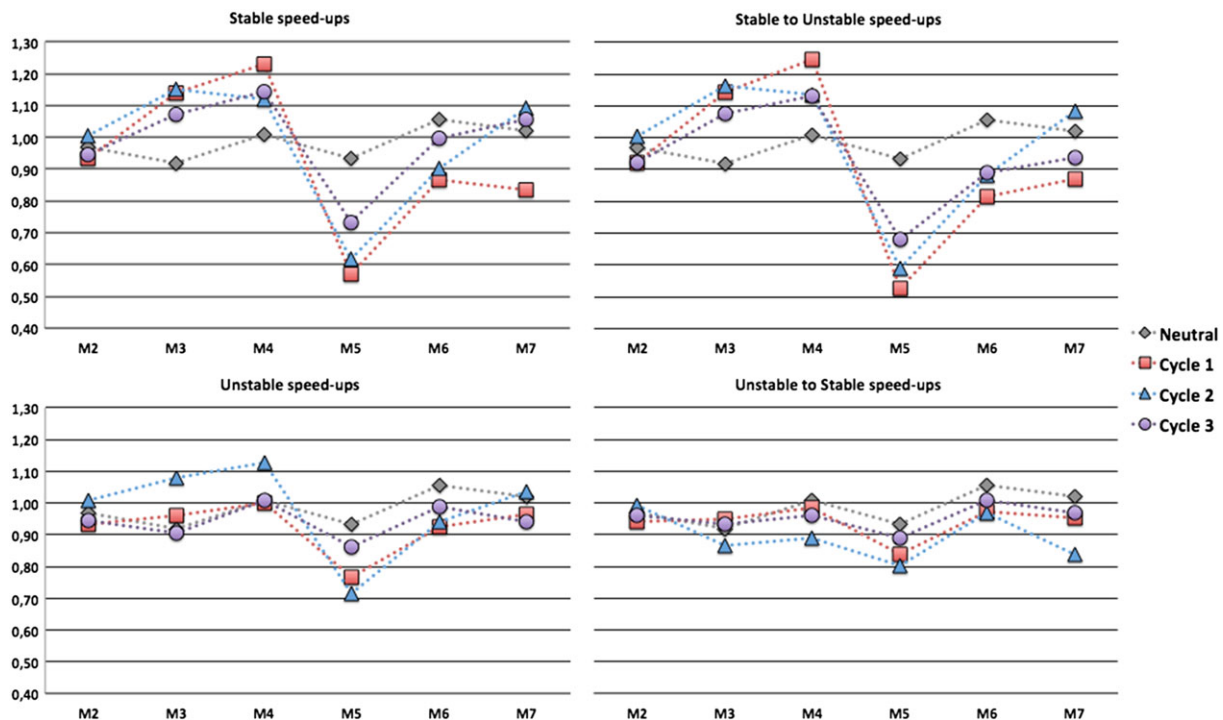[a]The analysis used the 90° sector for representativity.

FIGURE 11 Comparison of the speed-ups at masts M2 to M7 respect to mast M1 between the neutral case and the different diurnal cycles for the 90° sector. Neutral case in gray, results for the Cycle 1 in red, Cycle 2 in blue, and Cycle 3 in purple [Colour figure can be viewed at wileyonlinelibrary.com]

5 | CONCLUSIONS

A WRA methodology built on DC URANS simulations has been proposed and evaluated. This methodology introduces thermal stability as an additional parameter to account for thermal stratification effects in the wind field. The proposed methodology is physically more complex and computationally more expensive than the classical neutral steady-state assumption. However, this new methodology is able to capture wind flow behaviors that are not captured by steady-state neutral simulations. At Puebla site, the obtained differences between stable and unstable stratified flow fields were remarkable. In the stable stratified class, the obtained results showed a significant wind speed-up gradient in the western part of the domain, which is not captured by the neutral simulation. Directly related to this, the WPD distribution over the RoI is in closer agreement with mast observations in all stability classes and, particularly, in the final frequency-weighted aggregated results. At Puebla, the results obtained using the proposed methodology showed an averaged absolute error reduction on WPD from 30.1% to 13.0% with respect to the neutral ABL assumption. It has also been shown that the obtained results have a small dependence on the DC parameters.

This study has shown the potential of the DC methodology. Although the obtained results are encouraging, future studies should address some critical aspects to build a more robust methodology. The sensitivity to the different choices of parameters in the DC need to be studied in more detail. Another possibility is to move towards a more realistic DC that would leave some rather arbitrary choices out of the methodology, for example, using DCs more representative of the region under study. This could be achieved by linking the methodology with statistical weather classification techniques. In addition to that, a more realistic temperature distribution should be imposed over the ground, for example, using a temperature field depending on the insolation angle and terrain elevation.

ORCID

Jordi Barcons http://orcid.org/0000-0001-5550-1986
Matias Avila http://orcid.org/0000-0003-2248-7676
Arnau Folch http://orcid.org/0000-0002-0677-6366

REFERENCES

1. Ayotte KW. Computational modelling for wind energy assessment. *J Wind Eng Ind Aerodyn*. 2008;96(10-11):1571-1590. https://doi.org/10.1016/j.jweia.2008.02.002

2. Troen I, Lundtang Petersen E. European wind atlas, Denmark, Risø National Laboratories; 1989. http://orbit.dtu.dk/files/112135732/European-Wind-Atlas.pdf. Accessed April 5, 2017.

3. Taylor PA, Walmsley JL, Salmon JR. A simple model of neutrally stratified boundary-layer flow over real terrain incorporating wave number-dependent scaling. *Boundary-Layer Meteorol*. 1983;26:169-189. https://doi.org/10.1007/BF00121541

4. Palma JMLM, Castro FA, Ribeiro LF, Rodrigues AH, Pinto AP. Linear and nonlinear models in wind resource assessment and wind turbine micro-siting in complex terrain. *J Wind Eng Ind Aerodyn*. 2008;96(12):2308-2326. https://doi.org/10.1016/j.jweia.2008.03.012

5. Avila M, Folch A, Houzeaux G, Eguzkitza B, Prieto L, Cabezon D. A Parallel CFD model for wind farms. *Procedia Comput Sci*. 2013;18:2157-2166. https://doi.org/10.1016/j.procs.2013.05.386

6. Hristov Y, Oxley G, Žagar M. Improvement of AEP predictions using diurnal CFD modelling with site-specific stability weightings provided from mesoscale simulation. *J of Phys Conf Ser*. 2014;524:012116. https://doi.org/10.1088/1742-6596/524/1/012116

7. Pieterse JEE, Harms TMM. CFD investigation of the atmospheric boundary layer under different thermal stability conditions. *J Wind Eng Ind Aerodyn*. 2013;121:82-97. https://doi.org/10.1016/j.jweia.2013.07.014

8. Koblitz T, Bechmann A, Sogachev A, Sørensen N, Réthoré PE. Computational fluid dynamics model of stratified atmospheric boundary-layer flow. *Wind Energy*. 2015;18:75-89. https://doi.org/10.1002/we.1684

9. Sogachev A, Kelly M, Leclerc MY. Consistent two-equation closure modelling for atmospheric research: buoyancy and vegetation implementations. *Boundary-Layer Meteorol*. 2012;145(2):307-327. https://doi.org/10.1007/s10546-012-9726-5

10. Castro FA, Silva Santos C, Lopes da Costa JC. One-way mesoscale-microscale coupling for the simulation of atmospheric flows over complex terrain. *Wind Energy*. 2015;18(7):1251-1272. https://doi.org/10.1002/we.1758

11. Veiga-Rodrigues C, Palma JMLM, Rodrigues ÁH. Atmospheric flow over a mountainous region by a one-way coupled approach based on reynolds-averaged turbulence modelling. *Boundary-Layer Meteorol*. 2016;159(2):407-437. https://doi.org/10.1007/s10546-015-0116-7

12. Avila M, Gargallo-Peiró A, Folch A. A CFD framework for offshore and onshore wind farm simulation. *J Phy Conf Ser*. 2017;854. https://doi.org/10.1088/1742-6596/854/1/012002

13. Vázquez M, Houzeaux G, Koric S, et al. Alya: multiphysics engineering simulation toward exascale. *J Comput Sci*. 2016;14:15-27. https://doi.org/10.1016/j.jocs.2015.12.007

14. Houzeaux G, Vázquez M, Aubry R, Cela JM. A massively parallel fractional step solver for incompressible flows. *J Comput Phys*. 2009;228(17):6316-6332. https://doi.org/10.1016/j.jcp.2009.05.019

15. Apsley D, Castro I. A limited-length-scale k-ε model for the neutral and stably-stratified atmospheric boundary layer. *Boundary-Layer Meteorol*. 1997;83(1):75-98. https://doi.org/10.1023/A:1000252210512

16. Panofsky HA, Dutton JA. *Atmospheric Turbulence. Models and Methods for Engineering Applications*. New York: Wiley; 1984.

17. Monin AS, Obukhov A. Basic laws of turbulent mixing in the surface layer of the atmosphere. *Contrib Geophys Inst Acad Sci USSR*. 1954;151:163-187.

18. Gargallo-Peiró A, Avila M, Owen H, Prieto-Godino L, Folch A. Mesh generation for atmospheric boundary layer simulation in wind farm design and management. *Procedia Eng*. 2015;124:239-251. https://doi.org/10.1016/j.proeng.2015.10.136

19. Gargallo-Peiró A, Avila M, Owen H, Prieto-Godino L, Folch A. Mesh generation, sizing and convergence for onshore and offshore wind farm atmospheric boundary layer flow simulation with actuator discs. *J Comput Phys*. 2018;375:209-227. https://doi.org/10.1016/j.jcp.2018.08.031

20. Svensson G, Holtslag AAM, Kumar V, et al. Evaluation of the diurnal cycle in the atmospheric boundary layer over land as represented by a variety of single-column models: the second GABLS experiment. *Boundary-Layer Meteorol*. 2011;140(2):177-206. https://doi.org/10.1007/s10546-011-9611-7

21. Sanz-Rodrigo J, Churchfield M, Kosovic B. A methodology for the design and testing of atmospheric boundary layer models for wind energy applications. *Wind Energy Sci*. 2017;2(1):35-54. https://doi.org/10.5194/wes-2-35-2017

22. Kumar V, Svensson G, Holtslag AAM, Meneveau C, Parlange MB. Impact of surface flux formulations and geostrophic forcing on large-eddy simulations of diurnal atmospheric boundary layer flow. *J Appl Meteor Climatol*. 2010;49(7):1496-1516. https://doi.org/10.1175/2010JAMC2145.1

23. Skamarock WC, Klemp JB, Dudhia J, et al. A description of the Advanced Research WRF Version 3, National Center for Atmospheric Research; 2008.

24. Hong S-Y, Lim J-OJ. The WRF single-moment 6-class microphysics scheme (WSM6). *J Korean Meteor Soc*. 2006;42(2):129-151.

25. Kain JS. The Kain-Fritsch convective parameterization: an update. *J Appl Meteor*. 2004;43:170-181.

26. Janjic ZI. The surface layer in the NCEP Eta Model. In: Eleventh Conference on Numerical Weather Prediction, Norfolk, VA, 19-23 August; Amer. Meteor. Soc.; 1996; Boston, MA. 354-355.

27. Chen F, Dudhia J. Coupling an advanced land surface–hydrology model with the penn state–NCAR MM5 modeling system. Part I: Model implementation and sensitivity. *Mon Wea Rev*. 2001;129:569-585.

28. Janjic ZI. The step-mountain eta coordinate model: further developments of the convection, viscous sublayer and turbulence closure schemes. *Mon Wea Rev*. 1994;122:927-945.

29. Mlawer EJ, Taubman SJ, Brown PD, Iacono MJ, Clough SA. Radiative transfer for inhomogeneous atmospheres: RRTM, a validated correlated-k model for the longwave. *J Geophys Res*. 1997;102:16663-16682.

30. Dudhia J. Numerical study of convection observed during the winter monsoon experiment using a mesoscale two-dimensional model. *J Atmos Sci*. 1989;46(20):3077-3107.